

# Calcination temperature dependence on the structural and electrical properties of bismuth orthoferrite (BiFeO<sub>3</sub>) ceramics

M. N. ABDILLAH, D. TRIYONO\*

*Department of Physics, Faculty of Mathematics and Natural Sciences, Universitas Indonesia, UI Depok, Depok 16424, Indonesia*

We study the effect of the calcination temperature on the structural, morphological, and electrical properties of bismuth orthoferrite (BiFeO<sub>3</sub>) ceramics. The analyzed materials were synthesized via sol-gel and sintering methods. Structural (PSA and XRD) and morphological (SEM) analyses confirmed the hexagonal *R3c*-phase, polycrystalline nature, the decrease in crystallite size and grain size with increasing calcination temperature. The complex impedance spectra show the grain and grain boundary contributions to the electrical conduction mechanism. The electrical conductivity exhibited a thermal activation mechanism and the activation energy is in the 0.30 – 0.50 eV range that increase with increasing calcination temperature.

(Received August 13, 2019; accepted February 15, 2021)

*Keywords:* BiFeO<sub>3</sub>, Sol-gel method, Nyquist plot, Dielectric constant

## 1. Introduction

Multiferroics exhibit multiple ferroic properties, such as ferroelectricity and ferromagnetism, when the system experiences structural distortion [1]. Bismuth orthoferrite (BiFeO<sub>3</sub>) is one such multiferroic material because of the coupling of its electrical and magnetic behaviors [1]. The multiferroic properties of BiFeO<sub>3</sub> (BFO) highlight its potential use in a broad range of applications such as data storage, spin valves, spintronics, quantum electromagnets, and microelectronic devices [2].

BFO has a rhombohedral perovskite structure that is usually described using its hexagonal axes, where the hexagonal *c*-axis is directed along the [111] axis of pseudocubic cell and the hexagonal cell consists of six formula units [3]. BFO contains two cations, namely, Bi<sup>3+</sup> (in the 6s<sup>2</sup> orbital state) and Fe<sup>3+</sup> (in the 3d<sup>5</sup> orbital state), which govern its conductivity and magnetic ordering behavior, respectively [4]. It also exhibits ferroelectric behavior below the Curie temperature,  $T_C = 1103$  K and antiferromagnetic behavior below the Neel temperature,  $T_N = 643$  K [5-6].

However, it is difficult to obtain single phase BFO because of the appearance of other phases, such as Bi<sub>2</sub>O<sub>3</sub>, Fe<sub>2</sub>O<sub>3</sub>, Bi<sub>2</sub>Fe<sub>4</sub>O<sub>9</sub> and Bi<sub>25</sub>FeO<sub>40</sub> [4,7]. Synthesis methods have been applied to decrease the appearance of a second phase. Chin Moo Cho, et al. reported a hydrothermal method in the presence of triethanolamine which reacted strongly with the Fe ions, resulting in single-phase BFO [8]. Feng Gao, et al. synthesized single-phase BFO via a simple sol-gel method using 2-methoxyethanol nitric acid, with polyethylene glycol employed as a dispersant [4].

The samples in this study were synthesized via a sol-gel method, and single-phase BFO was obtained by varying the calcination temperature. Therefore, providing an alternative to the above-mentioned methods [4, 7-8], we used citric acid, bismuth nitrate, and ferrite nitrate nonahydrate as precursors. We investigated the effect of the calcination temperature on the structural, morphological, and electrical properties of BFO.

## 2. Experimental details

BFO samples were prepared in powder form via the sol-gel technique. The high purity precursors (Bi(NO<sub>3</sub>)<sub>3</sub>·9H<sub>2</sub>O, Fe(NO<sub>3</sub>)<sub>3</sub>·5H<sub>2</sub>O, and citric acid monohydrate) with suitable stoichiometry amounts, were weighted and thoroughly mixed into a homogeneous solution. The solution was then stirred and heated under a certain condition (80°C, 500 rpm) to form the gel-phase. The obtained gel was heated in a furnace to form the powder-phase. The obtained powder-phase was calcined under different calcination conditions: 500°C (Sample A), 600°C (Sample B), and 700°C (Sample C). The calcined powder was then pressed into a pellet in a compacting system under 5 kPa pressure for 3 min and sintered at 800°C to form bulk-phase BFO.

The particle size distribution of the calcined samples was studied using a particle size analyzer (PSA; Zetasizer Nano Zsp). The structural parameters were determined using an X-Ray Diffractometer (XRD; PANalytical-XPert PRO) with a Cu K $\alpha$  radiation source that was operated over a broad range of Bragg angles ( $10^\circ \leq 2\theta \leq 90^\circ$ ) at a 0.004°/s scan rate and 0.02° step size. A more refined

analysis of the structural parameters was conducted using the Highscore Plus software. The surface morphology was investigated via scanning electron microscopy (SEM; FEI QUANTA 650). The electrical properties were characterized using a LCR-Meter Fluke-PM 6303, with a 100 Hz to 1 MHz frequency range and 30°C–225°C temperature range.

### 3. Results and discussion

#### 3.1. PSA analysis

The particle size distribution of all of the calcined samples is presented in Fig. 1. The average particle sizes of samples A, B, and C are approximately 474, 333, and 282 nm, respectively. The prepared samples are still in the nanoscale domain.

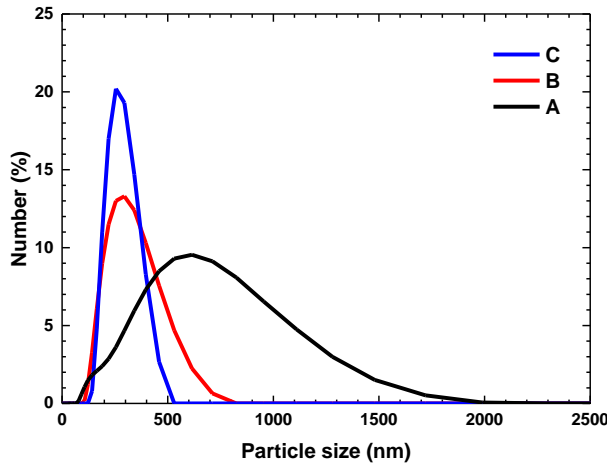


Fig. 1. Particle size distribution of the powder phase BFO at different calcination temperatures (color online)

#### 3.2. X-Ray diffraction analysis

The XRD pattern of bulk phase BFO is shown in Fig. 2. A small amount of second-phase material identified as Bi<sub>2</sub>Fe<sub>4</sub>O<sub>9</sub> is detected in the samples. The patterns of the bulk samples have been refined using the Highscore Plus software with the hexagonal structure and *R3c* space group. The influence of the calcination temperature on the structural parameters has been estimated and the results are listed in Table 1. The results show that the lattice and geometrical parameters are almost unchanged for the tested variations in calcination temperature. Fairly good values of  $\chi^2$  were obtained for each sample.

The average crystallite size was calculated using the Scherrer method [1]:

$$D = \frac{K\lambda}{\beta_{1/2} \cos \theta_{hkl}} \quad (1)$$

where  $\lambda$  is the wavelength of the x-rays (1.5405 Å),  $K = 0.89$ ,  $\beta_{1/2}$  is the full width at half maximum, and  $\theta$  is the

Bragg angle. The crystallite size (Table 1) decreases with increasing calcination temperature which indicates that the calcination temperature strongly affects the crystallite growth of bulk-phase BFO.

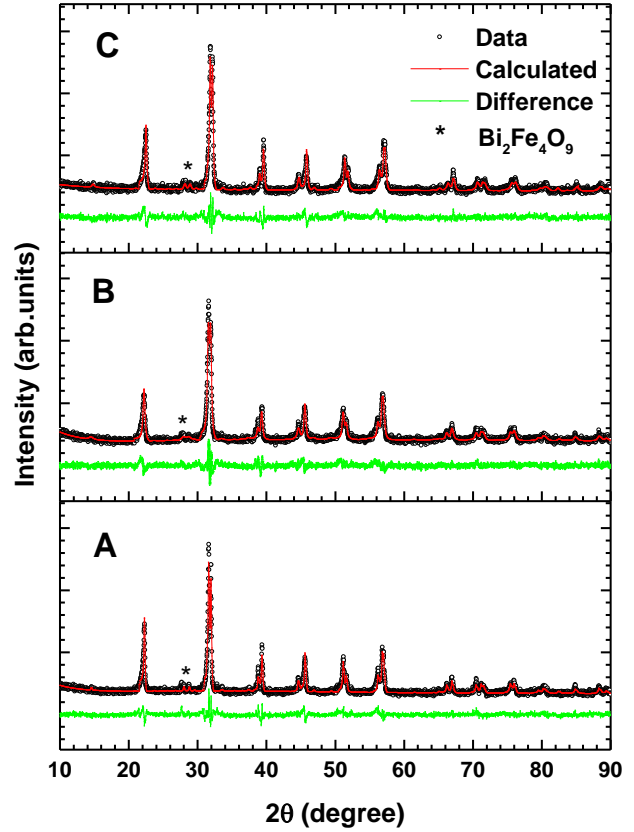


Fig. 2. XRD pattern of sintered bulk-phase BFO at different calcination temperatures (color online)

Table 1. Structural parameters of sintered bulk-phase BFO at different calcination temperatures

Crystallographic parameters					
Calcination temperature (°C)	a (Å)	c (Å)	Crystallite size (nm)		$\chi^2$
500	5.575	13.87	570		1.542
600	5.572	13.86	289		1.468
700	5.577	13.86	225		1.565
	Wyckoff position	Atomic position			Oxidation
		x	y	z	
Bi	6a	0	0	0.221	+3
Fe	6a	0	0	0	+3
O	18b	0.096	0.315	0.101	-2
Geometrical parameters					
Calcination temperature (°C)	Selected bond length (Å)		$t$	Bond angle (°)	
	Bi–O	Fe–O		Bi–O–Bi	Fe–O–Fe
500	2.279	1.954	1.166	110.9	155.6
600	2.276	1.952	1.165	110.8	155.8
700	2.270	1.955	1.161	111.2	155.6

The tolerance factor,  $t$ , was calculated using the Goldschmidt formula to explain the influence of the

calcination condition on the distortion of the crystal structure [9]:

$$t = \frac{(A - X)}{\sqrt{2(B - X)}} \quad (2)$$

where  $(A - X)$  is the bond length between La and O and  $(B - X)$  is the bond length between Fe and O. A hexagonal or tetragonal perovskite structure is formed for  $t > 1$  [9]. This indicates that the refinement results are consistent with the tolerance estimation given in Table 1, which makes sense because of the large ionic radii of the Bi-ions (131 pm) compared with those of the Fe-ions (69 pm), such that the hexagonal variants form in the perovskite structure [10].

### 3.3. SEM analysis

SEM images of the surface morphology of sintered bulk-phase BFO<sub>s</sub> at different calcination temperatures are shown in Fig. 3. The surface morphology reveals a non-uniform grain distribution that is separated by the grain boundary, indicating a typical polycrystalline nature. The dark grains come from the BFO, while the smaller-light colored grains are related with the Bi<sub>2</sub>Fe<sub>4</sub>O<sub>9</sub> as confirmed by XRD analysis. The images illustrate the tendency of the grains to decrease with increasing calcination temperature, whereas the grain boundaries increase. The average grain sizes are estimated to be approximately 2.5, 1.8, and 1.6 μm, for A, B, and C samples, respectively, which are consistent with crystallite sizes obtained via the XRD analysis.

### 3.4. Impedance plots at room temperature

The grain and grain boundary conduction mechanism in the materials can be identified using a Nyquist plot, as shown in Fig. 4a. Two distinct semicircular patterns are generally observed in the Nyquist plot, which represent the grain and grain boundary contributions [11-13]. The diameters of the semicircles increase with increasing calcination temperature. The larger diameter of the high frequency semicircle is indicative of low grain conduction and high grain resistivity. The effect of calcination temperature on the grain and grain boundary conduction mechanism is also shown in Fig. 4a, as both the grain and grain boundary resistivities increase with increasing calcination temperature.

The Nyquist plots are fitted using the equivalent circuit with a parallel combination of the resistance (R) and constant phase element in series with the grain boundary resistance and constant phase element ( $R_g - CPE_g$  and  $R_{gb} - CPE_{gb}$ ). The corresponding fitting parameters ( $R_g$  and  $R_{gb}$ ) that belong to the grains and grain boundary, respectively, are obtained and listed in Table 2. Grain resistance is the dominating factor in the electrical behavior of all of the samples since  $R_g > R_{gb}$ . It is also clear that the grain boundary resistance increases with increasing calcination temperature, indicating an increase

in charge carrier mobility during the conduction process [13].

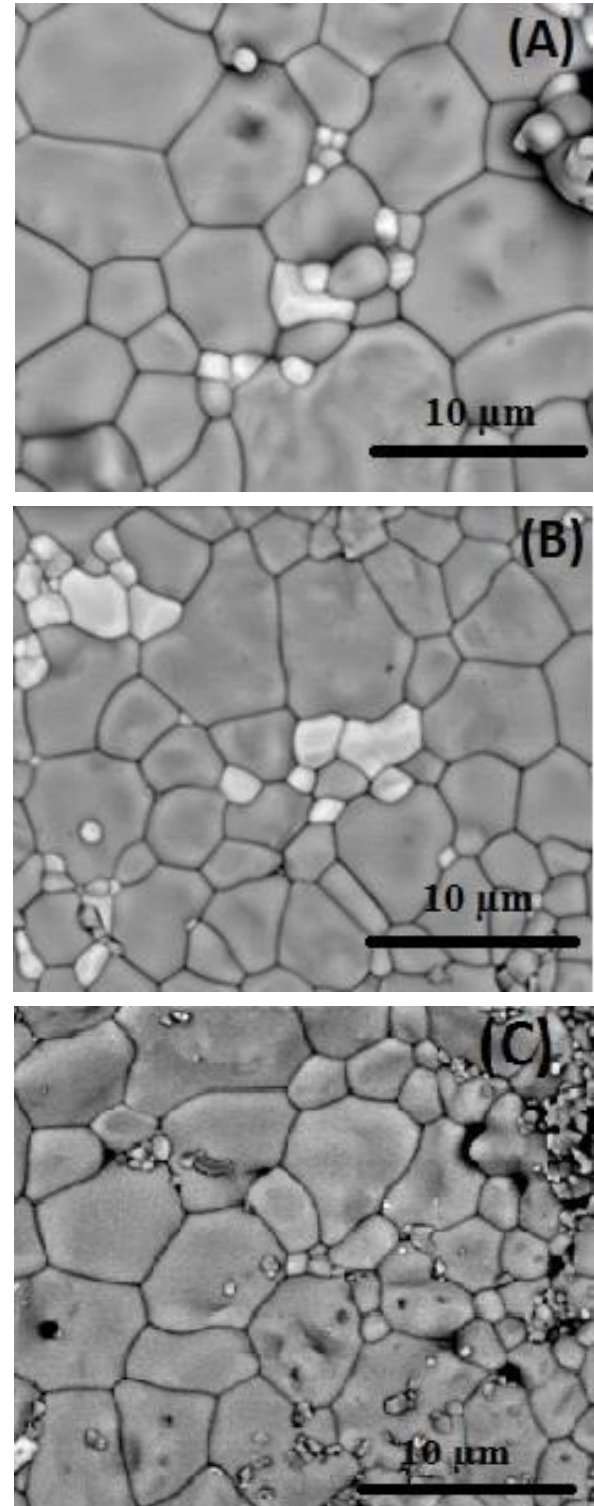


Fig. 3. SEM images of sintered bulk-phase BFO at different calcination temperatures: (a) sample A–500°C, (b) sample B–600°C, and (c) sample C–700°C

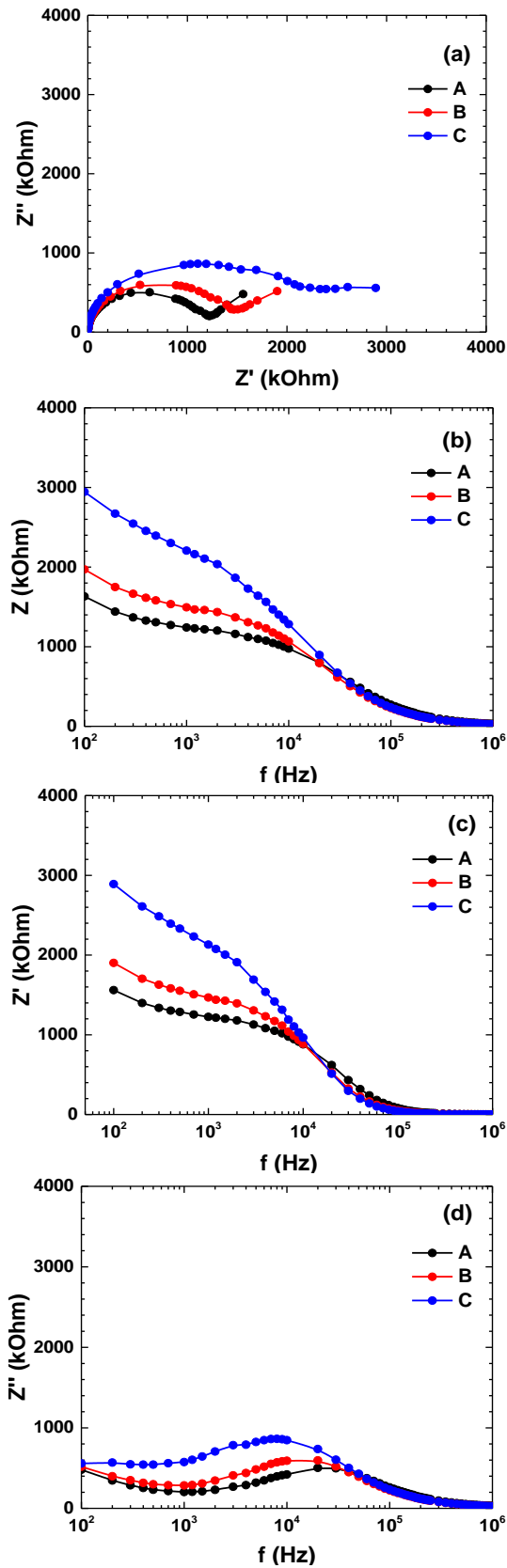


Fig. 4. (a) Nyquist plot, (b) absolute, (c) real, and (d) imaginary parts of the impedance for sintered bulk-phase BFO at room temperature (color online)

Table 2. Electrical parameters due to the grain and grain boundary, as obtained via fitting the data from all of the samples

Samples	$R_g$ (kOhm)	$R_{gb}$ (kOhm)
A	1288	1089
B	1461	1388
C	2727	2513

Bode plot of absolute impedance ( $Z$ ), real part ( $Z'$ ), and imaginary parts ( $Z''$ ) of impedance for all of the samples at room temperature are shown in Figs. 4b-d, respectively. It is clear that  $Z$  and  $Z'$  values decrease with increasing frequency and calcination temperature. The  $Z''$  value tends to increase until maximum value is reached and then starts to decrease rapidly as the frequency continues to increase. The maximum peak indicates the relaxation time when the relaxation mechanism occurs in the materials, which tends to shift to lower frequencies with increasing calcination temperature. This observation indicates that the calcination temperature accelerates the relaxation mechanism in the system.

### 3.5. Dielectric properties

The dielectric constant and tangent loss are two important parameters that are used to determine the dielectric properties of the material. These properties yield information on the relaxation and defects that occur in the material.

The dielectric constant for each sample is shown as a function of frequency in Fig. 5a, where the dielectric constant decreases with increasing frequency and then becomes frequency independent at higher frequencies. The dielectric constant decreases with increasing calcination temperature because of the decreasing grain size [13-14]. The tangent loss for each sample is shown as a function of frequency in Fig. 5b, where the tangent loss increases with increasing calcination temperature.

The temperature dependence of the dielectric constant for all of the samples at different calcination temperatures is shown in Fig. 6a, where the dielectric constant for all of the samples increases with increasing temperature. This behavior can be related to the thermal energy that is required to enhance the charge carrier mobility [15]. The variation in tangent loss as a function of calcination temperature is shown in Fig. 6b, where the tangent loss increases with increasing temperature until it reaches a maximum value and then starts to decrease as the temperature continues to increase, similar to that observed in ferroelectric materials [16]. The identified tangent loss maximum shifts to higher temperatures with increasing calcination temperature.

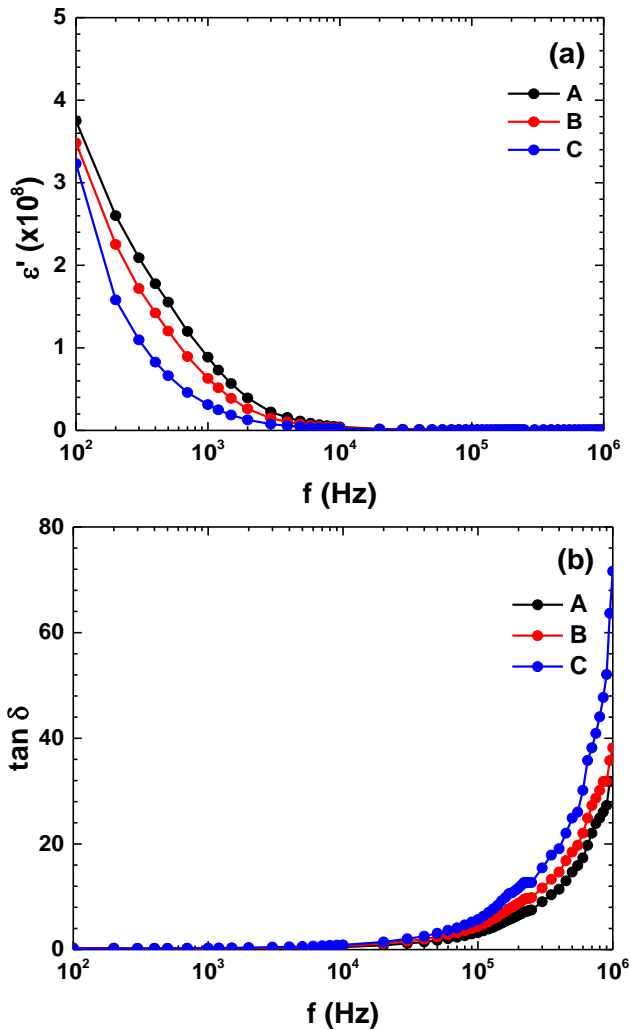


Fig. 5. Frequency dependence of the (a) dielectric constant and (b) tangent loss of sintered bulk phase BFO at room temperature (color online)

The frequency dependence of the dielectric constant at different calcination temperatures is shown in Fig. 7, where the dielectric constant decreases rapidly with increasing frequency in the low-frequency region and then becomes frequency independent in the high-frequency region. This decrease is caused by the reduction in the space charge polarization effect [17] since the high dielectric constant at lower frequencies is strongly related to the space charge polarization, which is caused by the migration of oxygen vacancies (charge carrier) at the grain boundary (defect) [15, 18]. The dielectric constant decrease with increasing calcination temperature at high temperatures, indicating that the calcination temperature plays an important role in the dielectric behavior of the BFO ceramic samples

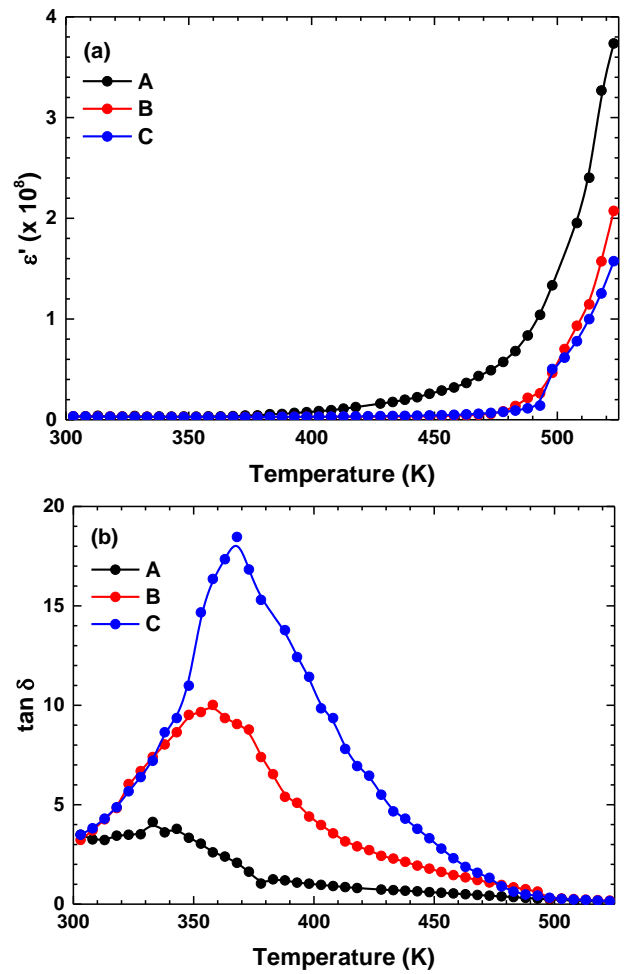


Fig. 6. Variation in the (a) dielectric constant and (b) tangent loss at 10 kHz for sintered bulk phase BFO as a function of temperature (color online)

### 3.6 Electrical properties

Nyquist plots of the sintered bulk-phase BFO samples at different calcination temperatures are shown in Fig. 8. Two semicircles are still preserved as the calcination temperature is increased, indicating that both the grain and grain boundary contribute to the electrical behavior at high temperatures for all of the samples. The diameters of the semicircles decrease with increasing temperature, indicating the negative temperature coefficient of resistance (NTCR) behavior of the compounds [15, 17].

The variation in electrical conductivity as a function of frequency is shown in Fig. 9. The conductivity remains relatively constant in the low-frequency region (DC conductivity) and varies linearly in the high frequency region (AC conductivity). The observed conductivities in the high and low-frequency regions are related to the hopping charge carrier and successive jumping of the mobile ion from one site to another inside the lattice, respectively [13, 19].

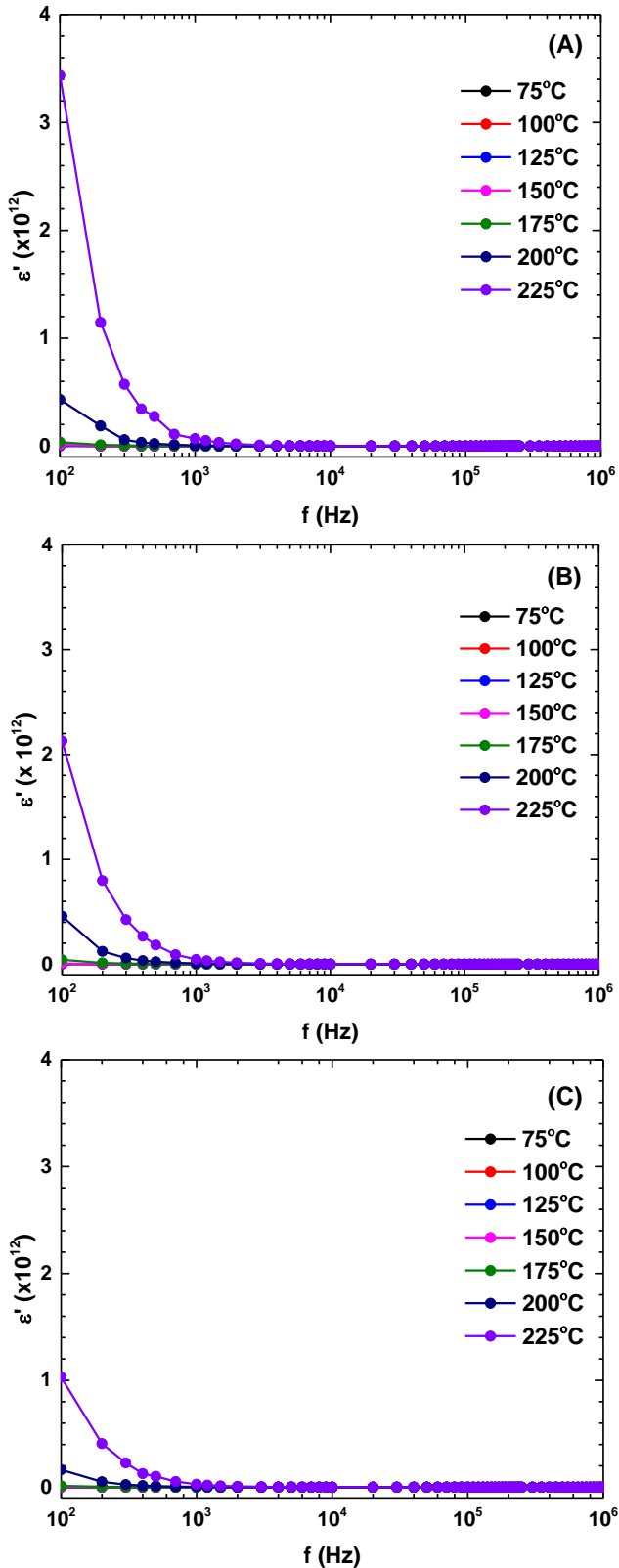


Fig. 7. Frequency dependence of the dielectric constant for sintered bulk phase BFO at different temperatures (color online)

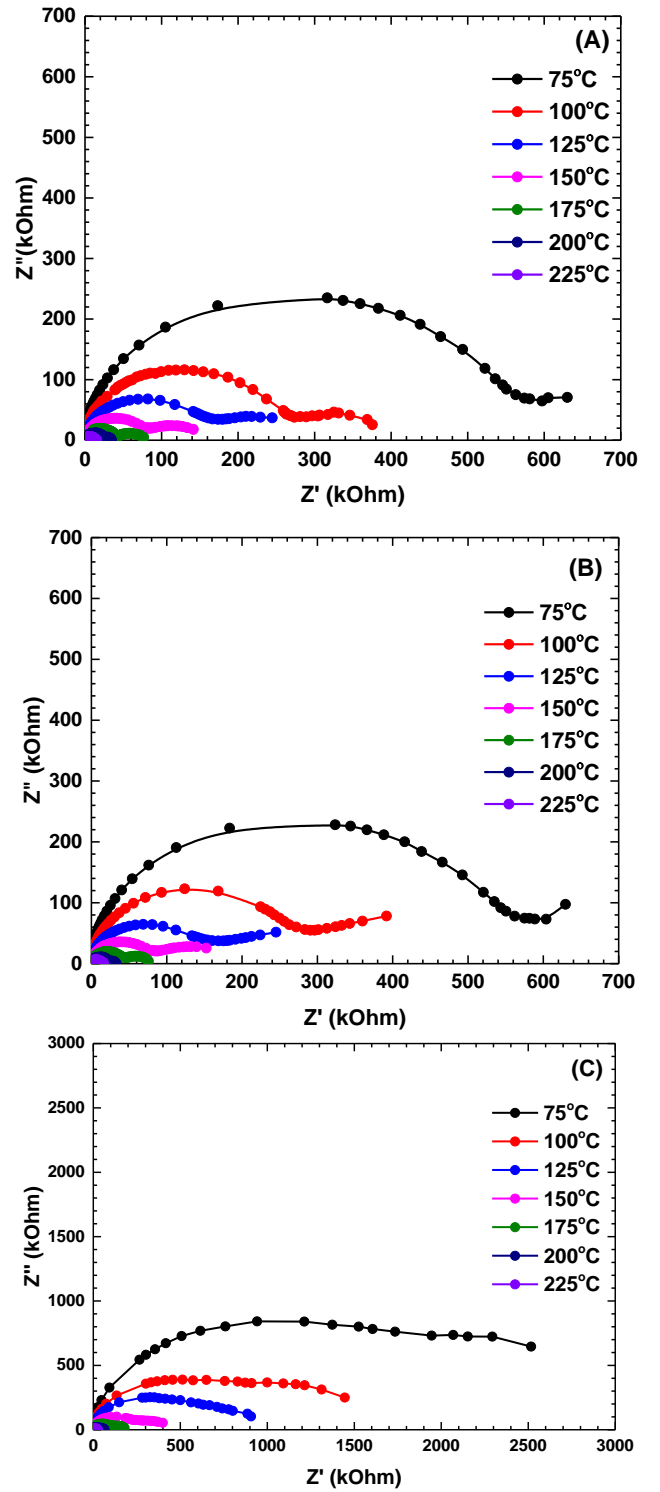


Fig. 8. Nyquist plots of sintered bulk phase BFO at different temperatures (color online)

The temperature dependence of DC conductivity for all of the samples has been estimated from the frequency dependence of the total conductivity, as shown in Figure 10. The DC conductivity increases with increasing temperature, suggesting a thermally activated conduction mechanism. The activation energies (which depend on the thermally activated process) for DC conduction were calculated via the Arrhenius law [16-18] with 0.34, 0.36,

and 0.47 eV estimated for samples (A), (B), and (C), respectively. The similarity between these activation energies implies that the conduction process may be attributed to the same type of charge carrier. Ionic conductivity dominates the conduction mechanism since the activation energy is  $< 1$  eV [17]. An increase in the activation energy generally indicates an increase in the resistance of the material [20, 21]. Therefore, the obtained activation energies are consistent with the analysis of the electrical parameters (Table 2), which indicate that the electrical behavior in the grain and grain boundary for all of the samples is the dominant conduction mechanism.

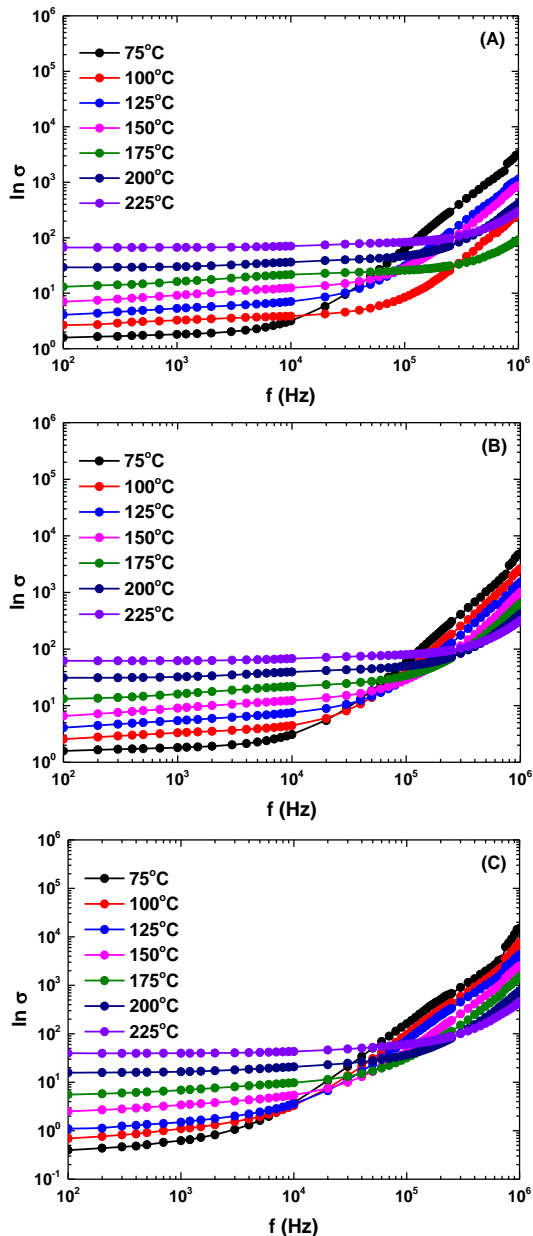


Fig. 9. Variations in the total conductivity of sintered bulk phase BFO as a function of frequency (color online)

At last, it is worth to mention here that the optimum calcined temperature which would give the best electrical behavior is 500°C (sample A) because this condition creates the highest dielectric constant and lowest

activation energy among these three different calcination temperature applied here.

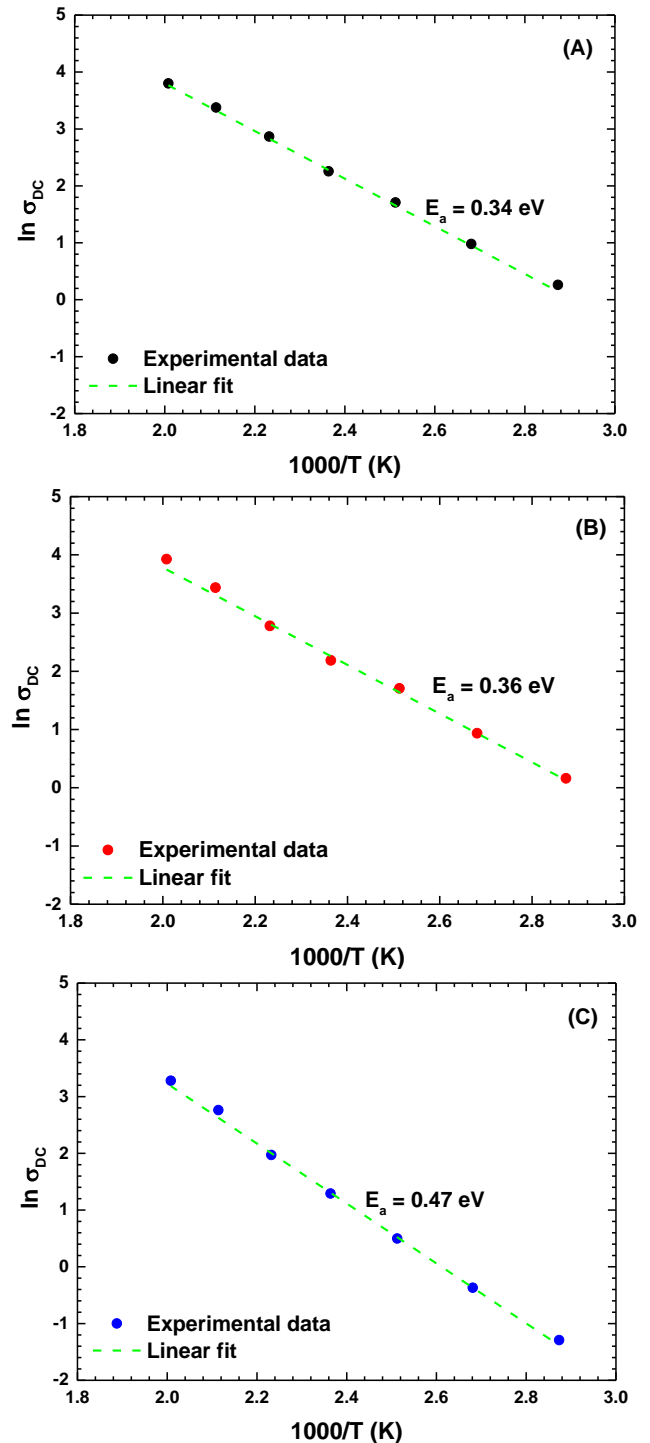


Fig. 10. Arrhenius plots for sintered bulk phase BFO (color online)

#### 4. Conclusions

BFO ceramics have been successfully synthesized via sol-gel and sintering methods. XRD analysis revealed that the samples possess a hexagonal symmetry ( $R3c$  space

group). The crystallite size increased with increasing calcination temperature. The SEM images showed homogeneously distributed grains with different sizes and shapes, indicating the polycrystalline nature of the samples. Impedance analysis revealed the contributions of the grain and grain boundary to the electrical mechanism, which is dependent on the calcination temperature. The dielectric constant decreases and the tangent loss increases with increasing calcination temperature. A typical NTCR behavior is observed in the analyzed BFO perovskite ceramic materials, and the DC conductivity increases with increasing temperature, which indicates that the conduction mechanism is thermally activated. The estimated activation energy is in the 0.30 – 0.50 eV range and increases with increasing calcination temperature. These outcomes indicate that the calcination temperature is a significant factor in the structure and electrical mechanism of BFO ceramics.

### Acknowledgements

D. Triyono thanks the University of Indonesia for financial support under PITTA Grant No. NKB-0437/UN2.R3.1/HKP.05.00/2019.

### References

- [1] S. Dash, R. N. P. Choudhary, P. R. Das, A. Kumar, *Can. J. Phys.* **93**, 738 (2015).
- [2] B. Bhushan, A. Basumallick, S. K. Bandopadhyay, N. Y. Vasanthacharya, D. Das, *J. Phys. D: Appl. Phys.* **42**, 065004 (2009).
- [3] J. G. Yu, H. G. Yu, B. Cheng, X. J. Zhao, J. C. Yu, W. K. Ho, *J. Phys. Chem. B.* **107**, 13871 (2003).
- [4] F. Gao, X. Y. Chen, K. B. Yin, S. Dong, Z. F. Ren, F. Yuan, T. Yu, Z. G. Zou, J. M. Liu, *Adv. Mater.* **19**, 2889 (2007).
- [5] Y. Li, T. Sritharan, S. Zhang, X. He, Y. Liu, T. Chen, *Appl. Phys. Lett.* **92**, 132908-1 (2008).
- [6] A. Z. Simoes, A. H. M. Gonzales, L. S. Cavalcante, C. S. Riccardi, E. Longo, J. A. Varela, *J. Appl. Phys.* **101**, 074108-1 (2007).
- [7] J. Chen, X. Xing, A. Watson, W. Wang, R. Yu, J. Deng, L. Yan, C. Sun, X. Chen, *Chem. Mater.* **19**(15), 3598 (2007).
- [8] C. M. Cho, J. H. Noh, I. S. Cho, J. S. An, K. S. Hong, J. Y. Kim, *J. Am. Ceram. Soc.* **11**, 3753 (2008).
- [9] R. J. D. Tilley, *Perovskite: Structure-Property Relationships*, Wiley, United Kingdom, 125 (2016).
- [10] V. A. Reddy, N. P. Pathak, R. Nath, *J. Alloys Comp.* **543**, 206 (2012).
- [11] A. Ben Jazia Kharrat, N. Moutia, K. Khirouni, W. Boujelben, *Mater. Res. Bull.* **105**, 75 (2018).
- [12] J. E. Bauerle, *J. Phys. Chem. Solids* **30**, 2657 (1969).
- [13] S. Dubey, O. Subohi, R. Kurchania, *Physica B* **521**, 73 (2017).
- [14] A. Khokhar, P. K. Goyal, O. P. Thakur, K. Sreenivas, *Ceram. Int.* **41**, 4189 (2015).
- [15] A. Raya, T. Basu, B. Behera, M. Kumar, R. Thapa, P. Nayak, *J. Alloys Compd* **768**, 198 (2018).
- [16] K. K. Bhargav, S. Ram, S. B. Rajumder, *J. Alloys Comp.* **638**, 334 (2015).
- [17] R. Kumari, N. Ahlawat, A. Agarwal, S. Sanghi, M. Sindhu, *J. Alloys Comp.* **695**, 3282 (2017).
- [18] D. Triyono, H. Laysandra, H. L. Liu, *J. Mater. Sci. Mater. Electron* **30**, 2512 (2019).
- [19] S. Padamavathi, J. Omprakash, C. S. Devi, M. Vithal, G. Prasad, G. Kumar, *Ferroelectrics* **474**, 83 (2015).
- [20] Z. Song, H. Liu, H. Hao, S. Zhang, M. Cao, Z. Yao, Z. Wang, W. Hu, Y. Shi, B. Hu, *IEEE Transactions on Ultrasonics, Ferroelectrics, and Frequency Control* **62**, 609 (2015).
- [21] G. Y. Yang, E. C. Dickey, C. A. Randall, D. E. Barber, P. Pinceloup, M. A. Henderson, R. A. Hill, J. J. Beeson, D. J. Skamser, *J. Appl. Phys.* **96**, 7492 (2004).

\*Corresponding author: djoko.triyono@ui.ac.id